ELSEVIER

Engineering Analysis with Boundary Elements 30 (2006) 949–962

ENGINEERING ANALYSIS with BOUNDARY ELEMENTS

www.elsevier.com/locate/enganabound

Analysis of electrostatic MEMS using meshless local Petrov–Galerkin (MLPG) method

Romesh C. Batra[a,*], Maurizio Porfiri[b], Davide Spinello[a]

[a]Department of Engineering Science and Mechanics, MC0219, Virginia Polytechnic Institute and State University, Blacksburg, VA 24061, USA
[b]Department of Mechanical, Aerospace and Manufacturing Engineering, Polytechnic University, Brooklyn, NY 11201, USA

Received 27 January 2006; accepted 14 April 2006
Available online 6 September 2006

Abstract

We analyze electrostatic deformations of rectangular, annular circular, solid circular, and elliptic micro-electromechanical systems (MEMS) by modeling them as elastic membranes. The nonlinear Poisson equation governing their deformations is solved numerically by the meshless local Petrov–Galerkin (MLPG) method. A local symmetric augmented weak formulation of the problem is introduced, and essential boundary conditions are enforced by introducing a set of Lagrange multipliers. The trial functions are constructed by using the moving least-squares approximation, and the test functions are chosen from a space of functions different from the space of trial solutions. The resulting nonlinear system of equations is solved by using the pseudoarclength continuation method. Presently computed values of the pull-in voltage and the maximum pull-in deflection for the rectangular and the circular MEMS are found to agree very well with those available in the literature; results for the elliptic MEMS are new.

Keywords: Micro-electromechanical systems; Pull-in instability; Meshless method; Pseudoarclength continuation method

1. Introduction

Recent technological developments and increasing market demand have opened promising research opportunities and engineering priorities in the field of micro-mechanics. The study of electrostatically actuated micro-electromechanical systems (MEMS) is a special branch of micro-mechanics. These MEMS are widely used in switches, micro-mirrors and micro-resonators. At the microscopic scale, high-energy densities and large forces are available, and the electrostatic actuation may dominate over other kinds of actuation.

Most of the electrostatically actuated MEMS consist of an elastic plate suspended over a stationary rigid plate. The plates are conductive and a dielectric material fills the gap between them. An applied electric voltage between the two plates results in the deflection of the elastic plate, and a consequent change in the MEMS capacitance. The applied electrostatic voltage has an upper limit, beyond which the electrostatic Coulomb force is not balanced by the elastic restoring force in the deformable plate, the two plates snap together and the MEMS collapses. This phenomenon, called pull-in instability, was simultaneously observed experimentally by Taylor [1], and Nathanson et al. [2]. The accurate estimation of the pull-in voltage is crucial in the design of electrostatically actuated MEMS device. In particular, in micro-mirrors [3] and micro-resonators [4] the designer avoids this instability in order to achieve stable motions; on the other hand in switching applications [5] the designer exploits this effect to optimize the performance of the device.

A simple model for estimating the pull-in parameters proposed in [2] is based on a lumped mass–spring system. This model qualitatively describes the pull-in phenomenon but it overestimates the pull-in voltages for many applications [6]. A possible extension of the lumped model consists of modeling the suspended plate as a membrane, and discarding the fringing electric fields. As discussed in [7], the membrane approximation is accurate and reliable for many MEMS devices such as micro-pumps made of thin

*Corresponding author. Tel.: +1 540 231 6051; fax: +1 540 231 4574.
E-mail addresses: rbatra@vt.edu (R.C. Batra), mporfiri@poly.edu (M. Porfiri), dspinell@vt.edu (D. Spinello).

0955-7997/$ - see front matter © 2006 Elsevier Ltd. All rights reserved.
doi:10.1016/j.enganabound.2006.04.008

glassy polymers, and grating light valves comprised of stretched thin ribbons. More refined linear and nonlinear models have been studied in [8,9].

Solutions by the shooting method (see e.g. [10, Chapter 7] for a discussion, and a list of references) can be obtained only for particular MEMS geometries that exhibit specific symmetries [11], that allow for the reduction of two-dimensional (2-D) to 1-D problems. However, it has been found in [12] that these simplifications may miss some unstable branches. Indeed, for an annular circular membrane the solution after the pull-in instability may break the symmetry inherited by the domain shape, loading, and boundary conditions. Therefore, it is crucial to develop accurate and reliable numerical methods for determining the pull-in instability parameters, and study, for arbitrary geometries, the MEMS behavior beyond the pull-in instability. Bao and Mukherjee [13] and Chyuan et al. [14] have employed the boundary element method to analyze MEMS.

Recently, considerable research in computational mechanics has been devoted to the development of meshless methods. One objective of these methods is to eliminate, or at least alleviate the difficulty of meshing and remeshing the entire structure, by only adding nodes at or deleting nodes from desired locations in the structure. Meshless methods may also alleviate some other problems associated with the finite element method, such as locking and element distortion. In many applications, they provide smooth and accurate approximate solutions with a reduced number of nodes. Therefore, only a few variables are needed in numerical models.

Meshless methods include the element-free Galerkin [15], hp-clouds [16], the reproducing kernel particle (RPK) [17], the smoothed particle hydrodynamics [18], the diffuse element [19], the partition of unity finite element [20], the natural element [21], meshless Galerkin using radial basis functions [22], the meshless local Petrov–Galerkin (MLPG) [23], and the modified smoothed particle hydrodynamics (MSPH) [24]. All of these methods, except for the MLPG, the MSPH, and the collocation, use shadow elements for evaluating integrals in the governing weak formulations [25].

The MLPG method has been successfully applied to several linear problems in mechanics: static linear plane elasticity [23]; vibrations of elastic planar bodies [26]; static analysis of thin plates [27]; static analysis of beams [28]; vibrations of cracked beams [41]; static analysis of functionally graded materials [29]; analysis of dynamic thermomechanical deformations of functionally graded materials [30]; analysis of axisymmetric transient heat conduction in a bimaterial disk [31]; and wave propagation in a segmented linear elastic bar [32]. Nonlinear problems analyzed with the MLPG method include adiabatic shear banding in thermoviscoelastoplastic materials [33], and the analysis of pull-in instability in micro-beams [34].

In order to completely eliminate a background mesh, the MLPG method is based on a local weak formulation of the governing equations and employs meshless interpolations for both the trial and the test functions. The trial functions are constructed by using the moving least squares (MLS) [35] approximation which relies on the location of scattered points in the body. In the Petrov–Galerkin formulation, test functions may be chosen from a different space than the space of trial solutions. Thus, several variations of the method may be obtained (see e.g. [25] for details).

Here we use the MLPG method to investigate the behavior of electrostatically actuated MEMS modeled as elastic membranes, and the method of Lagrange multipliers to impose displacement-type boundary conditions. Hence, a local symmetric augmented weak formulation (LSAWF) of the problem is introduced. Trial functions in the weak formulation are constructed using the MLS approximation, and weight functions in the MLS framework are chosen as test functions (MLPG1, [25]). In order to find the MEMS deformations beyond the pull-in instability the pseudoarclength continuation method (see e.g. [36,37]) is employed for solving the system of nonlinear equations resulting from the MLPG formulation. The method is applied to four distinct geometries: a rectangle, a circular disk, an annular disk, and an elliptic disk. In the first case, the effect of partial electrodes is studied, and computed results are compared with those obtained with the shooting method applied to the problem derived by generalizing the approach of [7] to partially electroded plates. In the second case, the computed results are validated by comparing them with those of [38]. For the annular circular disk, when symmetry breaking occurs, and no solution by the shooting method is available, the computed solution is compared with the finite-difference solution of [12]. To the authors' knowledge, the elliptic geometry has not been studied thus far. Here, the effect of the ellipse aspect ratio on the pull-in instability of the MEMS is investigated, and MLPG results are compared with those obtained by solving the 2-D boundary-value problem by the finite-difference method.

The rest of the paper is organized as follows. In Section 2 we present governing equations of the electrostatically actuated MEMS. In Section 3 we describe the MLPG method, including the LSWAF, the resulting set of nonlinear equations for the fictitious nodal deflections, and the pseudoarclength method. Computed solutions are presented in Section 4, and comparisons are made with available results. Conclusions are summarized in Section 5. In Appendix A we review the MLS approximation for constructing basis functions, and in Appendix B we give a brief description of confocal elliptic coordinates.

2. Governing equations

A schematic sketch of the problem studied is shown in Fig. 1. We assume that (i) both plates are perfect conductors, and are separated by a dielectric layer of permittivity $\in$, (ii) the bottom plate is rigid, and the top one is flexible, and can be modeled as a membrane, (iii) the membrane is either clamped or free on the

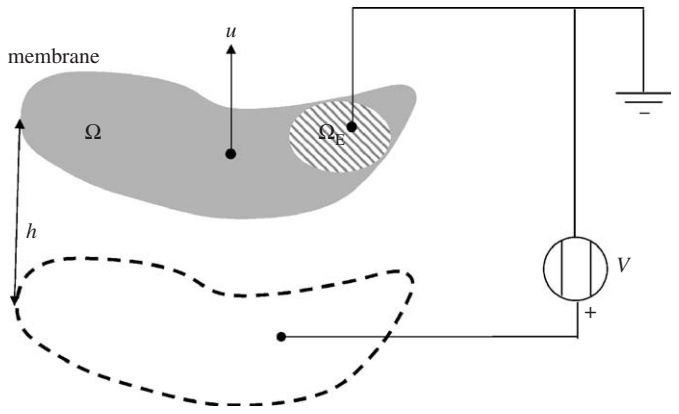

Fig. 1. Geometry of the Micro-electromechanical system.

boundary, (iv) a potential difference V exists between the two plates, (v) electric fringing fields are negligible (see e.g. [7]), and (vi) the uniform initial gap, h, between the two plates is much smaller than a typical linear dimension of the membrane. Under these assumptions the governing equation for the deflection u of the membrane becomes

$$T \triangle u(\mathbf{x}) = f_{\mathrm{E}}(u(\mathbf{x}), \mathbf{x}), \quad \mathbf{x} \in \Omega. \tag{1}$$

Here Ω is the membrane domain, $\mathbf{x}$ a generic point, T the tension in the membrane, $\triangle$ the Laplacian operator, and f_{E} the electrostatic force on the top plate. The electrostatic load is given by

$$f_{\mathrm{E}}(u(\mathbf{x}), \mathbf{x}) = \frac{\in V^2}{2h^2} \frac{\delta(\mathbf{x})}{(1 + u(\mathbf{x})/h)^2},$$

where

$$\delta(\mathbf{x}) = \begin{cases} 1, & \mathbf{x} \in \Omega_{\mathrm{E}}, \\ 0, & \mathbf{x} \notin \Omega_{\mathrm{E}} \end{cases}$$

and Ω_{E} is the membrane part where the electric force is effective.

We nondimensionalize the deflection by the initial gap h, the space coordinates by the characteristic domain length L, and obtain

$$\triangle u = \lambda \frac{\delta}{(1+u)^2}, \quad \lambda = \frac{\in V^2 L^2}{2h^3 T}, \tag{2}$$

where we have used the same symbols to indicate nondimensional quantities as were used earlier for dimensional quantities. Because of the term $(1+u)^2$ the problem is nonlinear.

3. Meshless method

3.1. Local symmetric augmented weak formulation

We rewrite the nonlinear Poisson equation (2) as

$$\triangle u = \lambda g(u, \mathbf{x}), \tag{3}$$

where

$$g(u, \mathbf{x}) = \frac{\delta(\mathbf{x})}{(1+u)^2}.$$

The boundary of the domain Ω is partitioned into two disjoint parts:

$$\partial\Omega = \Gamma_u \cup \Gamma_{\mathbf{n}}, \quad \overset{\circ}{\Gamma}_u \cap \overset{\circ}{\Gamma}_{\mathbf{n}} = \emptyset.$$

On Γ_u essential homogeneous boundary conditions are prescribed, that is

$$u(\mathbf{x}) = 0, \quad \mathbf{x} \in \Gamma_u,$$

while on $\Gamma_{\mathbf{n}}$ natural homogeneous boundary conditions are imposed, that is

$$\nabla u(\mathbf{x}) \cdot \mathbf{n}(\mathbf{x}) = 0, \quad \mathbf{x} \in \Gamma_{\mathbf{n}},$$

where $\mathbf{n}$ is the outward unit normal.

We partition the boundary Γ_u into σ connected parts, say $\Gamma_u^{(1)}, \ldots, \Gamma_u^{(\sigma)}$. In order to enforce the essential boundary conditions we introduce σ Lagrange multipliers fields $\gamma^{(1)}, \ldots, \gamma^{(\sigma)}$, each of them being defined on the corresponding part $\Gamma_u^{(\alpha)}$ of Γ_u.

We introduce a LSAWF of the problem on a subdomain Ω_{S} of the domain Ω:

$$-\int_{\Omega_{\mathrm{S}}} \nabla u \cdot \nabla \tilde{u}\, \mathrm{d}\Omega - \int_{\Omega_{\mathrm{S}} \cap \Omega_{\mathrm{E}}} \lambda g(u, \mathbf{x})\, \tilde{u}\, \mathrm{d}\Omega + \int_{L_{\mathrm{S}}} \nabla u \cdot \mathbf{n}\, \tilde{u}\, \mathrm{d}\Gamma + \sum_{\alpha=1}^{\sigma} \left(\int_{\Gamma_{\mathrm{S}u}^{(\alpha)}} u\, \tilde{\gamma}^{(\alpha)} \mathrm{d}\Gamma + \int_{\Gamma_{\mathrm{S}u}^{(\alpha)}} \tilde{u}\, \gamma^{(\alpha)} \mathrm{d}\Gamma \right) = 0. \tag{4}$$

Here, as illustrated in Fig. 2, $\Gamma_{\mathrm{S}u}^{(\alpha)}$ is the intersection of $\partial\Omega_{\mathrm{S}}$ with $\Gamma_u^{(\alpha)}$, L_{S} is the part of $\partial\Omega_{\mathrm{S}}$ enclosed in the domain Ω, $\tilde{u}$ and $\tilde{\gamma}^{(\alpha)}$ are smooth test functions defined, respectively, in Ω_{S} and $\Gamma_{\mathrm{S}u}^{(\alpha)}$. The homogeneous natural boundary conditions have been embedded in the weak formulation of the problem.

In the MLPG method test functions and trial solutions are chosen from different spaces, and the test function need not vanish where essential boundary conditions are specified. In order to simplify the algebraic work, we select test functions $\tilde{u}$ which vanish on the inner boundary L_{S};

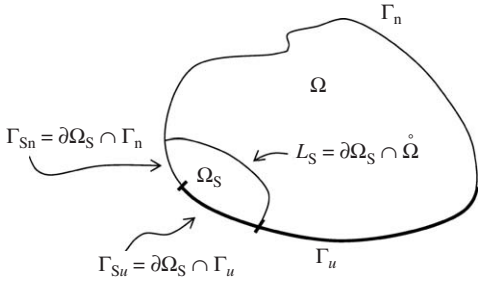

Fig. 2. Sketch of the domain, subdomains and different boundaries.

therefore the LSAWF (4) reduces to

$$-\int_{\Omega_S}\nabla u\cdot\nabla\tilde{u}\,d\Omega-\int_{\Omega_S\cap\Omega_E}\lambda g\,\tilde{u}\,d\Omega+\sum_{\alpha=1}^{\sigma}\left(\int_{\Gamma_{Su}^{(\alpha)}}u\,\tilde{\gamma}^{(\alpha)}d\Gamma+\int_{\Gamma_{Su}^{(\alpha)}}\tilde{u}\gamma^{(\alpha)}\,d\Gamma\right)=0. \tag{5}$$

Subdomains Ω_S are taken to be circles in order to facilitate the numerical evaluation of integrals.

3.2. Discrete nonlinear formulation

In order to seek an approximate solution of the nonlinear problem, we use 2-D MLS basis functions[1] (see Appendix A) to express the trial solution in terms of nodal unknowns, $\hat{u}_1,\ldots,\hat{u}_N$. Note that the MLS basis functions do not have the Kronecker delta property. Therefore nodal unknowns, $\hat{u}_1,\ldots,\hat{u}_N$, do not equal values of the trial solution at the nodes. The Lagrange multiplier field $\gamma^{(\alpha)}$ is approximated by 1-D MLS basis functions constructed from nodes lying on the curve $\Gamma_u^{(\alpha)}$. We emphasize that only nodes belonging to $\Gamma_u^{(\alpha)}$ are employed for constructing the field $\gamma^{(\alpha)}$. Therefore

$$(\gamma^{(\alpha)})^h=\sum_{\beta=1}^{\nu^{(\alpha)}}\hat{\gamma}_\beta^{(\alpha)}\chi_\beta^{(\alpha)},$$

where $\nu^{(\alpha)}$ is the number of nodes belonging to $\Gamma_u^{(\alpha)}$, $\chi_\beta^{(\alpha)}$'s are 1-D MLS basis functions, and $\hat{\gamma}_\beta^{(\alpha)}$'s are fictitious nodal values. We collect $\hat{\gamma}_\beta^{(\alpha)}$'s into σ distinct vectors $\hat{\boldsymbol{\gamma}}^{(1)},\ldots,\hat{\boldsymbol{\gamma}}^{(\sigma)}$, and denote the total number of Lagrange multiplier nodes by $N_L:=\sum_{\alpha=1}^{\sigma}\nu^{(\alpha)}$.

In order to derive $N+N_L$ equations for nodal unknowns $\hat{\mathbf{u}}$ and $\hat{\boldsymbol{\gamma}}^{(1)},\ldots,\hat{\boldsymbol{\gamma}}^{(\sigma)}$, we consider in (5) N subdomains $\Omega_{S1},\ldots,\Omega_{SN}$, and $N+N_L$ independent test functions: $\tilde{u}_1,\ldots,\tilde{u}_N$, and $\tilde{\gamma}_1^{(\alpha)},\ldots,\tilde{\gamma}_{\nu^{(\alpha)}}^{(\alpha)}$, $\alpha=1,\ldots,\sigma$. The discrete nonlinear equations obtained from (5) are

$$\mathbf{K}\hat{\mathbf{u}}+\lambda\mathbf{G}(\hat{\mathbf{u}})+\sum_{\alpha=1}^{\sigma}\mathbf{R}^{(\alpha)}\hat{\boldsymbol{\gamma}}^{(\alpha)}=\mathbf{0}, \tag{6a}$$

$$\mathbf{V}^{(\alpha)}\hat{\mathbf{u}}=\mathbf{0},\quad\alpha=1,\ldots,\sigma, \tag{6b}$$

where

$$[\mathbf{K}]_{ij}=-\int_{\Omega_S^i}\nabla\psi_j\cdot\nabla\tilde{u}_i\,d\Omega,\quad i,j=1,\ldots,N, \tag{7a}$$

$$[\mathbf{G}(\hat{\mathbf{u}})]_i=-\int_{\Omega_S^i\cap\Omega_E}g(u^h,\mathbf{x})\,\tilde{u}_i\,d\Omega,\quad i=1,\ldots,N, \tag{7b}$$

$$[\mathbf{R}^{(\alpha)}]_{i\beta}=\int_{\Gamma_{Su}^{i\,(\alpha)}}\chi_\beta^{(\alpha)}\tilde{u}_i d\Gamma,\quad i=1,\ldots,N,\ \beta=1,\ldots,\nu^{(\alpha)}, \tag{7c}$$

$$[\mathbf{V}^{(\alpha)}]_{\beta j}=\int_{\Gamma_{Su}^{\beta\,(\alpha)}}\psi_j\,\tilde{\gamma}_\beta^{(\alpha)}d\Gamma,\quad\beta=1,\ldots,\nu^{(\alpha)},\ j=1,\ldots,N. \tag{7d}$$

[1]The boundary $\partial\Omega$ of the 2-D domain Ω is approximated by piecewise straight lines connecting adjacent nodes on it.

For subdomains having the shape of a sector of a circle, integrals in Eqs. (7a)–(7d) can be computed by the Gauss quadrature rule.

In the MLPG1 method the test function $\tilde{u}_i$ for the ith node is chosen to be the weight function W_i used in the MLS approximation, but of a different support. That is,

$$\tilde{u}_i(\mathbf{x})=W_i(\eta_i\mathbf{x}),$$

where η_i is a positive number representing the ratio of the supports of the test, and the weight functions for the ith node. Test functions for the Lagrange multipliers are chosen to be the test functions $\tilde{u}_i$'s restricted to the boundary of the domain.

Let rows of the $(N-N_L)\times N$ matrix $\mathbf{Y}$ be comprised of $(N-N_L)$ linearly independent null vectors of the $N_L\times N$ matrix $\mathbf{V}$ obtained by appending rows of matrices $\mathbf{V}^{(\alpha)}$'s, and set

$$\hat{\mathbf{u}}=\mathbf{Y}^{\mathrm{T}}\mathbf{u}. \tag{8}$$

Substitution from (8) into (6b) gives

$$\mathbf{V}^{(\alpha)}\mathbf{Y}^{\mathrm{T}}\mathbf{u}=\mathbf{0},\quad\alpha=1,\ldots,\sigma,$$

which are identically satisfied for every $(N-N_L)$-vector $\mathbf{u}$. Similarly, let rows of the $(N-N_L)\times N$ matrix $\mathbf{X}$ equal $(N-N_L)$ linearly independent null vectors of the $N_L\times N$ matrix $\mathbf{R}^{\mathrm{T}}$ obtained by appending columns of matrices $\mathbf{R}^{(\alpha)}$'s, and transposing the entire matrix. Then

$$\mathbf{X}\mathbf{R}^{(\alpha)}=\mathbf{0},\quad\alpha=1,\ldots,\sigma.$$

Premultiplying both sides of Eq. (6a) by $\mathbf{X}$ and substituting from (8) we obtain the following reduced system of $(N-N_L)$ nonlinear equations for $\mathbf{u}$:

$$\bar{\mathbf{K}}\mathbf{u}+\lambda\bar{\mathbf{G}}(\mathbf{u})=\mathbf{0}, \tag{9}$$

where

$$\bar{\mathbf{K}}=\mathbf{X}\mathbf{K}\mathbf{Y}^{\mathrm{T}},\quad\bar{\mathbf{G}}(\mathbf{u})=\mathbf{X}\,\mathbf{G}(\mathbf{Y}^{\mathrm{T}}\mathbf{u}).$$

Having found $\mathbf{u}$ from (9), $\hat{\mathbf{u}}$ is computed from (8).

4. Pseudoarclength continuation method

The system of nonlinear equations (9) may not admit a unique solution $\mathbf{u}$ for an arbitrary value of the parameter λ. We use the pseudoarclength continuation method (see e.g. [36,37]) to solve Eqs. (9). It enables one to find the complete bifurcation path and the symmetry breaking bifurcation. The pseudoarclength method exhibits the stability and the reliability of the new displacement pull-in extraction (DPIE) scheme presented in [39], since it does not treat the applied voltage as a given parameter but as an unknown. Furthermore, it detects symmetry breaking bifurcations which seem not to be predicted by the DPIE algorithm.

In this method a new parameter s is added so that λ and $\mathbf{u}$ are considered functions of s. If the solution $(\mathbf{u}_k,\lambda_k)$ of Eqs. (9) is known at $s=s_k$, the solution $(\mathbf{u}_{k+1},\lambda_{k+1})=(\mathbf{u}_k+\Delta\mathbf{u}_{k+1},\lambda_k+\Delta\lambda_{k+1})$ at the abscissa $s_{k+1}=s_k+\Delta s_{k+1}$

is found by solving the system of equations:

$$\bar{\mathbf{K}}\mathbf{u}_{k+1} + \lambda_{k+1}\bar{\mathbf{G}}(\mathbf{u}_{k+1}) = \mathbf{0},$$
$$(\mathbf{u}_{k+1} - \mathbf{u}_k)^{\mathrm{T}}\mathbf{M}\dot{\mathbf{u}}_k + (\lambda_{k+1} - \lambda_k)\dot{\lambda}_k - \Delta s_{k+1} = 0, \tag{10}$$

where $\mathbf{M}$ is a symmetric positive definite matrix, and a superimposed dot indicates derivative with respect to s. In many cases (see e.g. [36,37]), $\mathbf{M}$ is chosen to be the identity matrix, but for the present problem, numerical experiments have shown that more stable solutions are obtained by choosing

$$\mathbf{M} = \boldsymbol{\Psi}^{\mathrm{T}}\boldsymbol{\Psi},$$

where $\boldsymbol{\Psi}$ is defined by (27) in Appendix A. This implies that the arc length is computed by using the actual nodal values, rather than the fictitious ones.

The solution of the set (10) of nonlinear equations, for the unknowns $\Delta\mathbf{u}_{k+1}$ and $\Delta\lambda_{k+1}$, is found by using Newton's iterations. Hence the generic μth iteration is

$$\begin{bmatrix} \bar{\mathbf{K}}^{(\mu)}_{k+1} & \bar{\mathbf{G}}(\mathbf{u}^{(\mu)}_{k+1}) \\ (\dot{\mathbf{u}}_k)^{\mathrm{T}}\mathbf{M} & \dot{\lambda}_k \end{bmatrix} \begin{bmatrix} \Delta\mathbf{u}^{(\mu)}_{k+1} \\ \Delta\lambda^{(\mu)}_{k+1} \end{bmatrix} = - \begin{bmatrix} \bar{\mathbf{K}}\mathbf{u}^{(\mu)}_{k+1} + \lambda^{(\mu)}_{k+1}\bar{\mathbf{G}}(\mathbf{u}^{(\mu)}_{k+1}) \\ (\mathbf{u}^{(\mu)}_{k+1} - \mathbf{u}_k)^{\mathrm{T}}\mathbf{M}\dot{\mathbf{u}}_k + (\lambda^{(\mu)}_{k+1} - \lambda_k)\dot{\lambda}_k - \Delta s_{k+1} \end{bmatrix}, \tag{11}$$

where $(\Delta\mathbf{u}^{(\mu)}_{k+1}, \Delta\lambda^{(\mu)}_{k+1})$ indicates the μth solution increment; $(\mathbf{u}^{(\mu)}_{k+1}, \lambda^{(\mu)}_{k+1})$ is the updated solution at the $(\mu-1)$th iteration, i.e.

$$\mathbf{u}^{(\mu)}_{k+1} = \mathbf{u}_k + \sum_{h=1}^{\mu-1}\Delta\mathbf{u}^{(h)}_{k+1}, \quad \lambda^{(\mu)}_{k+1} = \lambda_k + \sum_{h=1}^{\mu-1}\Delta\lambda^{(h)}_{k+1}.$$

$\bar{\mathbf{K}}^{(\mu)}_{k+1}$ is the tangent stiffness at the $(\mu-1)$th iteration, i.e.

$$\bar{\mathbf{K}}^{(\mu)}_{k+1} = \bar{\mathbf{K}} + \lambda^{(\mu)}\mathbf{X}\mathbf{D}^{(\mu)}_{k+1}\mathbf{Y}^{\mathrm{T}},$$

with

$$[\mathbf{D}^{(\mu)}_{k+1}]_{ij} = \int_{\Omega^i_{\mathrm{S}}\cap\Omega_{\mathrm{E}}} \frac{2}{(1 + \boldsymbol{\psi}(\mathbf{x})^{\mathrm{T}}\mathbf{Y}^{\mathrm{T}}\mathbf{u}^{(\mu)}_{k+1})^3}\psi_j\tilde{u}_i\,\mathrm{d}\Omega.$$

Iterations are performed until the infinity norm of the incremental deflection field, and the incremental λ is below a prescribed tolerance ε_{T}. That is, iterations are performed till

$$\max\left[\sup_{\mathbf{x}\in\Omega}[\boldsymbol{\psi}(\mathbf{x})^{\mathrm{T}}\mathbf{Y}^{\mathrm{T}}\Delta\mathbf{u}^{(\mu)}_{k+1}], \Delta\lambda^{(\mu)}_{k+1}\right] < \varepsilon_{\mathrm{T}}.$$

Once the solution $(\mathbf{u}_{k+1}, \lambda_{k+1})$ has been found, the direction vector $(\dot{\mathbf{u}}_{k+1}, \dot{\lambda}_{k+1})$, needed for the subsequent iteration is determined by solving

$$\begin{bmatrix} \bar{\mathbf{K}}^{(\bar{\mu}_{k+1})}_{k+1} & \bar{\mathbf{G}}(\mathbf{u}^{(\bar{\mu}_{k+1})}_{k}) \\ (\dot{\mathbf{u}}_k)^{\mathrm{T}}\mathbf{M} & \dot{\lambda}_k \end{bmatrix} \begin{bmatrix} \dot{\mathbf{u}}_{k+1} \\ \dot{\lambda}_{k+1} \end{bmatrix} = \begin{bmatrix} \mathbf{0} \\ 1 \end{bmatrix},$$

where $\bar{\mu}_{k+1}$ is the number of iterations required for the solution to converge. The direction vector is then rescaled according to

$$(\dot{\mathbf{u}}_{k+1})^{\mathrm{T}}\mathbf{M}\dot{\mathbf{u}}_{k+1} + (\dot{\lambda}_{k+1})^2 = 1.$$

The length Δs_{k+2} for the next step is determined from the knowledge of the length Δs_{k+1} and the iteration number $\bar{\mu}_{k+1}$ using the following simple adaptive scheme

$$\Delta s_{k+2} = \Delta s_{k+1}\sqrt{\frac{\tau}{\bar{\mu}_{k+1}}},$$

where τ represents the desired number of iterations for the convergence of Newton's method. The parameter τ is chosen in such a way that if Newton's method converges rapidly the step size is increased, while if Newton's method converges slowly the step size is decreased [36].

The pseudoarclength algorithm is started by assuming that for $s_0 = 0$ the solution is the pair $(\mathbf{u}_0, \lambda_0) = (\mathbf{0}, 0)$, and computing the solution $\mathbf{u}_1$ for a given small λ_1 with the standard Euler method resulting from linearizing (9) about $(\mathbf{u}_0, \lambda_0)$. Once the solution corresponding to this small electrostatic force is computed, the direction vector $(\dot{\mathbf{u}}_1, \dot{\lambda}_1)$ is estimated by the linear approximation

$$\dot{\mathbf{u}}_1 = \frac{1}{\Delta s_1}(\mathbf{u}_1 - \mathbf{u}_0), \quad \dot{\lambda}_1 = \frac{1}{\Delta s_1}(\lambda_1 - \lambda_0),$$

where the initial arc length is

$$\Delta s_1 = \sqrt{(\mathbf{u}_1)^{\mathrm{T}}\mathbf{M}\mathbf{u}_1 + (\lambda_1)^2}.$$

We note that when the tangent stiffness matrix, $\bar{\mathbf{K}}$, becomes singular the whole matrix is generally nonsingular unless a bifurcation occurs. This means that the pull-in instability may be detected, and the MEMS post-instability behavior analyzed.

When a bifurcation occurs the whole matrix on the left-hand side of Eq. (11) becomes singular, and crossing the bifurcation point implies a change in the sign of the determinant of this matrix (see [36]). In this case, the bifurcation point is determined by using the secant method, and the bifurcation path is followed by using the normal vector to the original path as an initial estimate of the direction vector.

5. Results

We compare results for a rectangular, a circular, an annular circular, and an elliptic MEMS from the MLPG method with those obtained using either the shooting method or the finite-difference method. For the elliptic MEMS, we investigate the effect of the ellipse aspect ratio on the pull-in instability. To the authors' knowledge, no earlier results are available for the elliptic MEMS.

For the nondimensional problem (3) parameters compared are λ_{PI} and $\|u_{\mathrm{PI}}\|_\infty$, and, when a symmetry breaking bifurcation occurs, λ_{SB} and $\|u_{\mathrm{SB}}\|_\infty$. λ_{PI} and $\|u_{\mathrm{PI}}\|_\infty$ indicate, respectively, the value of the parameter λ for which the pull-in instability occurs, and the corresponding infinity norm of the deflection field; λ_{SB} and $\|u_{\mathrm{SB}}\|_\infty$ represent, respectively, the highest λ for which a symmetry breaking bifurcation occurs, and the corresponding infinity norm of the deflection field.

For a specific MEMS, the dimensional value of the pull-in voltage (symmetry breaking bifurcation) is obtained by substituting λ_{PI} (λ_{SB}) into (2), while the dimensional value of the membrane deflection at the pull-in instability (symmetry breaking bifurcation) is obtained by multiplying $\|u_{PI}\|_\infty$ ($\|u_{SB}\|_\infty$) by the initial gap h.

The MLS approximation (see Appendix A) uses linear monomial basis, $m = 3$. The size r_i of the support of a weight function varies with the problem, and other constants defining weight functions are $k = 1$, $c_i = r_i/4$. The integration is performed by using nine quadrature points for each line integral, and 9×9 quadrature points for each 2-D subdomain. Values of basis functions at quadrature points are stored in the computer memory to economize on the CPU time. The pseudoarclength continuation is started with $\lambda_1 = 0.1$, $\tau = 3$, and the tolerance ε_T is set equal to 10^{-6}. If the convergence is not achieved in 10 Newton's iterations the incremental arc length Δs is reduced by a factor of 2, and the algorithm is restarted from that point. In the neighborhood of the pull-in instability, more steps are needed to accurately estimate the pull-in parameters.

5.1. Rectangular MEMS

We consider a rectangular MEMS of unit length, width equal to 1/8, clamped on edges $x^1 = 0, 1$, and free on edges $x^2 = 0, 1/8$. We assume that the electrostatic force is exerted only for $x^1 \in (\varepsilon, 1 - 2\varepsilon)$.

5.1.1. Reduction of boundary-value problem to initial-value problem

Following [7], we assume that the solution is only a function of x^1, and is symmetric with respect to the line $x^1 = 1/2$, yielding the following 1-D nonlinear boundary-value problem:

$$u_1''(x^1) = 0, \quad x^1 \in (0, \varepsilon), \tag{12a}$$

$$u_2''(x^1) = \frac{\lambda}{(1 + u_2(x^1))^2}, \quad x^1 \in (\varepsilon, 1/2), \tag{12b}$$

$$u_1(0) = 0, \quad u_2'(1/2) = 0, \tag{12c}$$

$$u_1(\varepsilon) = u_2(\varepsilon), \quad u_1'(\varepsilon) = u_2'(\varepsilon), \tag{12d}$$

where a superimposed prime indicates derivative with respect to x^1.

The solution of the homogeneous equation (12a) for $x^1 \in (0, \varepsilon)$ is

$$u_1(x^1) = c_1 x^1 + c_2, \quad c_1, c_2 \in \mathbb{R}.$$

By imposing the first boundary condition in (12c), we obtain

$$c_2 = 0.$$

The interphase conditions (12d) give

$$u_2(\varepsilon) = c_1 \varepsilon, \tag{13a}$$

$$u_2'(\varepsilon) = c_1. \tag{13b}$$

Hence the constant c_1 may be eliminated, and the deflection field for $x^1 \in (\varepsilon, 1/2)$ is determined by solving the boundary-value problem

$$u_2''(x^1) = \frac{\lambda}{(1 + u_2(x^1))^2}, \quad u_2(\varepsilon) = u_2'(\varepsilon)\varepsilon,$$
$$u_2'(1/2) = 0. \tag{14}$$

The constant c_1 is subsequently determined by either (13a) or (13b).

Next, by generalizing the approach of [7] to partially electroded plates we convert the boundary-value problem to the initial-value problem

$$\frac{d^2 w}{d\eta^2} = \frac{1}{w^2}, \quad \frac{dw}{d\eta}(0) = 0, \quad w(0) = 1.$$

The above transformation is achieved by applying the change of variables:

$$\eta = b((\tfrac{1}{2} - \varepsilon) - x^1), \quad u^2(x^1) = aw(\eta) - 1,$$
$$a = \frac{1}{w(b(\frac{1}{2} - \varepsilon)) + \varepsilon b w'(b(\frac{1}{2} - \varepsilon))},$$

$$\lambda = \frac{b^2}{(w(b(\frac{1}{2} - \varepsilon)) + \varepsilon b w'(b(\frac{1}{2} - \varepsilon)))^3}. \tag{15}$$

We numerically solve the aforementioned initial-value problem with Mathematica using the built-in function NDSolve, obtain $w(\eta)$, and for every pair (w, b) we determine the corresponding pair $(u^2(x^1), \lambda)$, and the constant c_1. Once the deflection field is known on the entire strip we compute its infinity norm, which equals the mid-span deflection.

5.1.2. Numerical results and comparisons

For the solution of the 2-D boundary-value problem by the MLPG method, we use a regular grid of 33×5 nodes on the MEMS domain as shown in Fig. 3. Radii r_i of the support of each weight function (Eq. (28)) are set equal to 1/8. The subdomains of integration are determined by supports of test functions, and their radii are chosen equal to 1/32.

Fig. 4 exhibits the bifurcation diagram showing the infinity norm of the deflection versus the load parameter λ. We emphasize that beyond the pull-in voltage there is no steady state configuration where the two plates are separate. For different values of the parameter ε, we compare in Table 1 the MLPG solutions with those obtained by solving the problem by the method of Section 5.1.1. It is clear that values of λ_{PI} predicted by the MLPG method are very close to those obtained from the method of Section 5.1.1; the maximum difference between the two for $\varepsilon = 0.4$ equals 0.3%. The maximum deviation between the two values of $\|u_{PI}\|_\infty$ equals 1.28%, and occurs for $\varepsilon = 0.3$.

For $\varepsilon = 0$ and $\lambda = 1.19$, Fig. 5 gives the deflected shape of the MEMS for a configuration beyond the pull-in instability. The MLPG solution is independent of

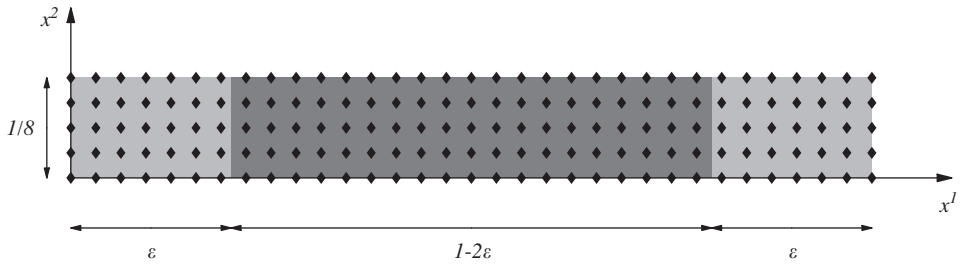

Fig. 3. Uniform grid of 33 × 5 nodes on the rectangular MEMS. The electrostatic force is effective in the shaded region.

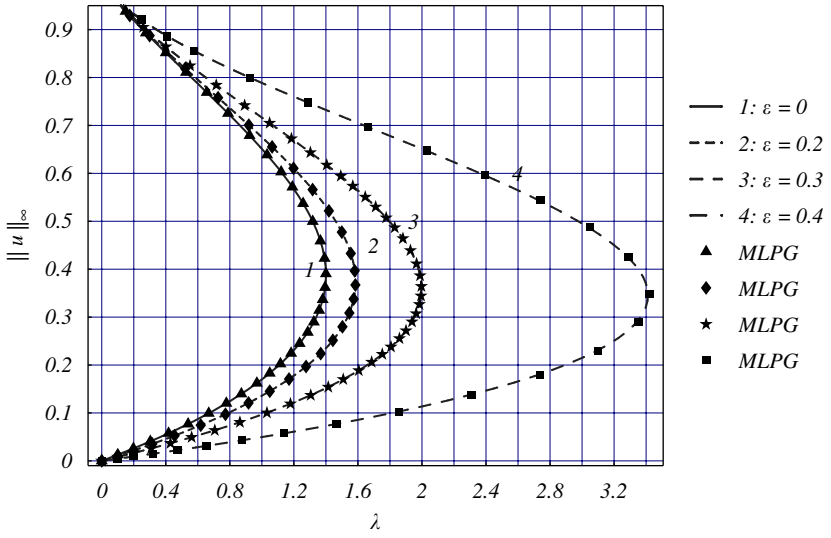

Fig. 4. For different values of ε, comparison of the bifurcation diagrams obtained with the method of Section 5.1.1 (solid line) and the MLPG method (polygons) for the rectangular MEMS.

Table 1
For the rectangular MEMS, comparison of the MLPG results with those obtained by the method of Section 5.1.1

ε	Method of Section 5.1.1		MLPG	
	λ_{PI}	$\|u_{PI}\|_\infty$	λ_{PI}	$\|u_{PI}\|_\infty$
0	1.400	0.3927	1.400	0.3885
0.2	1.584	0.3671	1.584	0.3671
0.3	1.996	0.3662	1.997	0.3615
0.4	3.412	0.3470	3.421	0.3475

the x^2 coordinate, and supports the assumption made in Section 5.1.1. The maximum deflection of the MEMS exceeds $\|u_{PI}\|_\infty$ because no constraint is imposed on the maximum deflection of a point. Deformed shapes of the membrane beyond the pull-in deflection may be unstable and hence physically unrealizable.

5.2. Circular disk

We consider a disk of unit radius clamped along its periphery.

5.2.1. Reduction of boundary-value problem to initial-value problem

Following [38] we assume that the solution is a function of the radial coordinate r only. Thus, the problem defined by Eq. (2) reduces to the following 1-D nonlinear boundary-value problem:

$$u''(r) + \frac{1}{r}u'(r) = \frac{\lambda}{(1+u(r))^2}, \quad u(1) = 0, \; u'(0) = 0, \qquad (16)$$

where a superimposed prime indicates derivative with respect to r.

We reduce the boundary-value problem (16) to the initial-value problem

$$\frac{d^2w}{d\eta^2} + \frac{1}{\eta}\frac{dw}{d\eta} = \frac{1}{w^2}, \quad \frac{dw}{d\eta}(0) = 0, \quad w(0) = 1,$$

by applying the following change of variables:

$$\eta = br, \quad u(r) = aw(\eta) - 1, \quad a = \frac{1}{w(b)}, \quad \lambda = \frac{b^2}{w(b)^3}.$$

As for the rectangular MEMS, we numerically solve the initial-value problem with Mathematica using the built-in function NDSolve, and for every pair (w, b) determine the

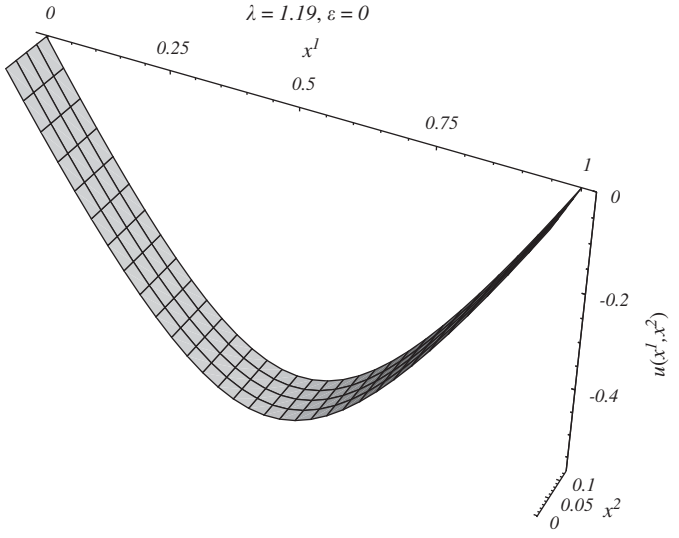

Fig. 5. Deformed shape of the rectangular MEMS with $\varepsilon = 0$ and $\lambda = 1.19$.

corresponding pair $(u(r), \lambda)$. Once the deflection field is known on the entire disk we compute its infinity norm, which equals the deflection of the disk center.

5.2.2. Numerical results and comparisons

Instead of considering the entire disk we analyze deformations of a quarter of the disk by using the grid of 86 nodes shown in Fig. 6. Here we do not assume that the deflection is independent of the circumferential coordinate ϑ. On straight boundaries we impose homogeneous natural boundary conditions arising from the symmetry of the problem. We thus tacitly neglect solutions that do not exhibit the presumed symmetries. The size r_i of the support of each weight function is chosen to be $2/3$. Subdomains of integration are determined by supports of test functions, and their radii are chosen equal to the distance between the chosen node and the one closest to it.

Fig. 7 shows the infinity norm of the deflection versus the load parameter λ. Results from the MLPG method and those from the technique of Section 5.2.1 are compared in Table 2; the difference between the two values of λ_{PI}, and $\|u_{\mathrm{PI}}\|_\infty$ equal 0.32% and 1.6%, respectively.

Fig. 8 depicts the deformed shape of a quarter of the disk for a voltage less than the pull-in voltage with the deflection at the center greater than the pull-in deflection. The computed deflection is found to be independent of the circumferential coordinate, and supports the assumption made in Section 5.2.1.

5.3. Annular disk

We consider an annular disk of inner radius 0.1, and outer radius 1 clamped along its inner and outer boundaries.

Following [12] we study only one-half of the annular domain, and impose homogeneous natural boundary conditions on the straight edges. We thus do not compute

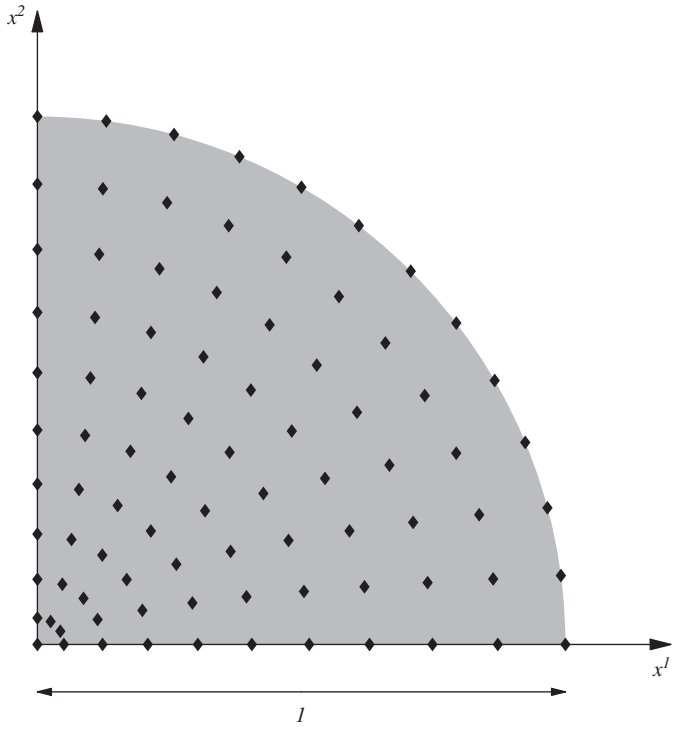

Fig. 6. Grid of 86 nodes on the quarter of disk.

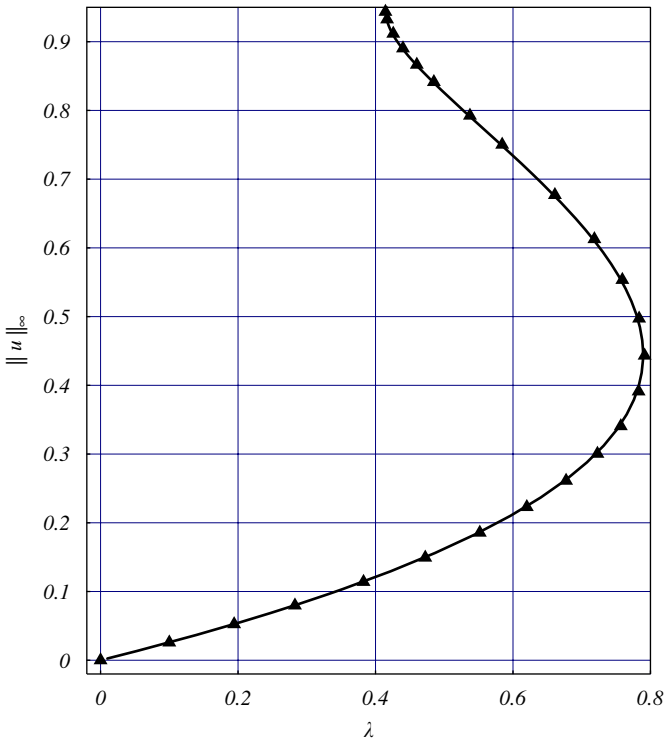

Fig. 7. Comparison of the bifurcation diagrams obtained with the method of Section 5.2.1 (solid line) and the MLPG method (triangles) for the circular MEMS.

solutions that are asymmetric about the horizontal axis. The symmetry breaks after the pull-in instability, and the bifurcated solution does not inherit the symmetry of the

Table 2
For the circular MEMS, comparison of the MLPG results with those from the method of Section 5.2.1

Method of Section 5.2.1		MLPG	
λ_{PI}	$\|u_{PI}\|_\infty$	λ_{PI}	$\|u_{PI}\|_\infty$
0.7890	0.4365	0.7915	0.4433

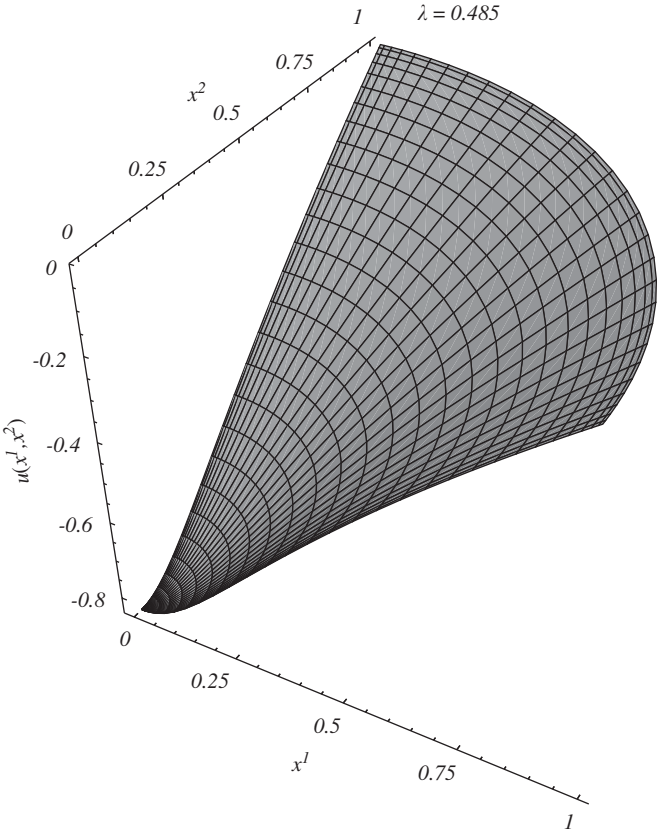

Fig. 8. Deformed shape of a quarter of the circular MEMS for $\lambda = 0.485$.

domain. We compare our results with those obtained in [12] by the finite-difference method using 1600 points.

In the MLPG implementation, we use the 165 nodes located as shown in Fig. 9. Values of weight functions parameters are the same as those for the circular disk problem studied in Section 5.2.

Fig. 10 exhibits the infinity norm of the deflection versus the load parameter λ. Numerical solutions from the MLPG and the finite-difference methods are compared in Table 3. The symmetry breaking voltage, λ_{SB}, is less than the pull-in voltage λ_{PI}, and the maximum difference between the corresponding values of λ_{PI}, $\|u_{PI}\|_\infty$ and λ_{SB} is 1.53%.

Figs. 11a and b report the symmetric, and the asymmetric deformed shapes of the annular disk after the pull-in, for $\lambda = 1.34$, and 1.18, respectively.

Fig. 12 depicts the variation of the pull-in parameters, λ_{PI} and $\|u_{PI}\|_\infty$, with the ratio (inner radius)/(outer radius),

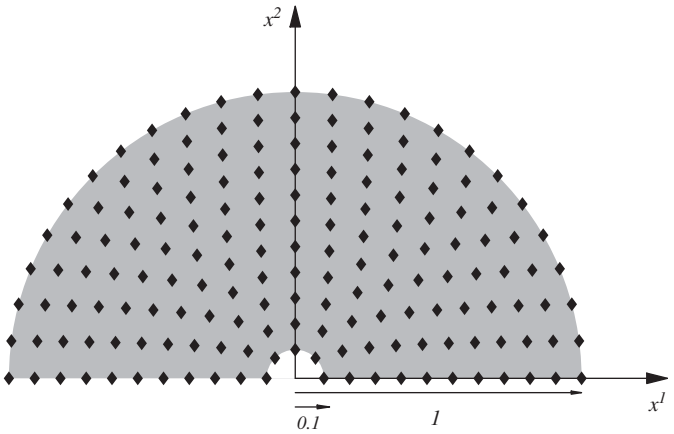

Fig. 9. Locations of 165 nodes on one-half of an annular disk.

keeping the outer radius at the constant value 1. The MLPG results are computed using ~165 nodes. The nondimensional pull-in voltage data are fitted with a quadratic polynomial (dashed line), and the corresponding nondimensional pull-in maximum deflections with a polynomial of degree zero (solid line). Expressions for the aforementioned polynomials are

$$\lambda_{PI} = 1.33 + 16.3\,\rho^2, \quad \|u_{PI}\|_\infty = 0.390,$$

where ρ is the ratio (inner radius)/(outer radius). Whereas the maximum pull-in deflection is nearly independent of the ratio of the inner to the outer radius of the MEMS, the pull-in voltage increases essentially quadratically with this ratio. Fig. 13 exhibits the dependence of symmetry breaking parameters, λ_{SB} and $\|u_{SB}\|_\infty$, upon the ratio of the inner to the outer radius of the annular disk. With increasing inner radii, the nondimensional pull-in voltage λ_{PI} significantly increases due to increased stiffness of the system, and the same holds for the nondimensional lowest symmetry breaking voltage, λ_{SB}. Whereas the nondimensional pull-in maximum deflection, $\|u_{PI}\|_\infty$, is virtually independent of the inner radius of the disk, the nondimensional symmetry breaking maximum deflection, $\|u_{SB}\|_\infty$, decreases with increasing inner radius. Expressions for the best fit polynomials in Fig. 13 are

$$\lambda_{SB} = 1.27 + 16.6\rho^2, \quad \|u_{SB}\|_\infty = 0.513 - 0.254\rho.$$

Fig. 14 shows the variation with the ratio ρ, of the quantity $(r^* - \rho)/(1 - \rho)$, where r^* is the ratio between the radial location of the nondimensional pull-in maximum displacement $\|u_{PI}\|_\infty$, and the outer radius of the ring. MLPG data are fitted with a quadratic polynomial (solid line) whose expression is

$$\frac{r^* - \rho}{1 - \rho} = 0.343 + 0.450\rho - 0.423\rho^2.$$

5.4. Elliptic disk

We consider an ellipse of semi-major axis $a = 1$, semi-minor axis b, and clamped along its periphery. We analyze

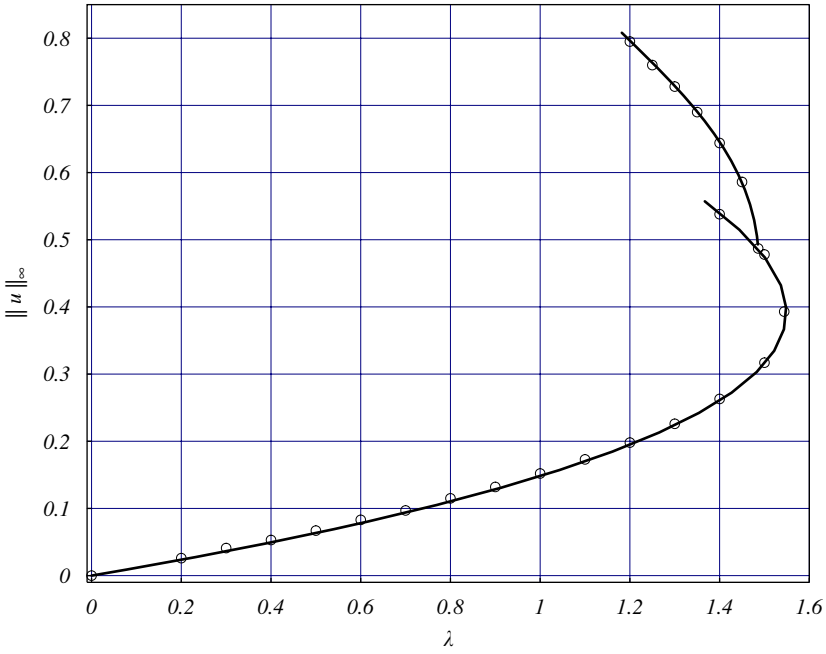

Fig. 10. Bifurcation diagram for the annular disk MEMS: finite-difference solution (empty circles) and MLPG computations (solid line).

Table 3
Comparison of the MLPG results with the finite-difference solution for the annular MEMS with inner radius equal to one-tenth of the outer radius

Finite-difference			MLPG		
λ_{PI}	$\|u_{PI}\|_\infty$	λ_{SB}	λ_{PI}	$\|u_{PI}\|_\infty$	λ_{SB}
1.544	0.393	1.486	1.548	0.399	1.485

one quarter of the ellipse, impose homogeneous natural boundary conditions on the straight edges, and investigate the effect of the aspect ratio b/a on the pull-in instability of the system. As before, we do not compute solutions that are asymmetric about either one of the two major axes of the ellipse.

We study four aspect ratios, namely $0.25, 0.5, 0.75$, and 0.95. We use the grids of $86, 87, 85$, and 94 nodes as shown in Figs. 15a–d. For a uniformly loaded elliptical membrane clamped on its edges, these nodal placements give an error of less than 0.7% in the maximum deflection with respect to the analytical solution

$$u^a(x^1, x^2) = \kappa\left(\left(\frac{x^1}{a}\right)^2 + \left(\frac{x^2}{b}\right)^2 - 1\right),$$
$$\kappa = 1\Big/\left(\frac{2}{a^2} + \frac{2}{b^2}\right). \tag{17}$$

Here, x^1 and x^2 are Cartesian coordinates aligned with the major and the minor axes of the ellipse. Values of weight functions parameters are the same as for the circular disk, and the annular disk problems studied in previous sections.

Fig. 16 shows pull-in bifurcation diagrams for four elliptic MEMS. Due to an increase in the stiffness of the system with a decrease in the aspect ratio, the nondimensional pull-in voltage increases significantly with a decrease in b/a. Results are compared with finite-difference

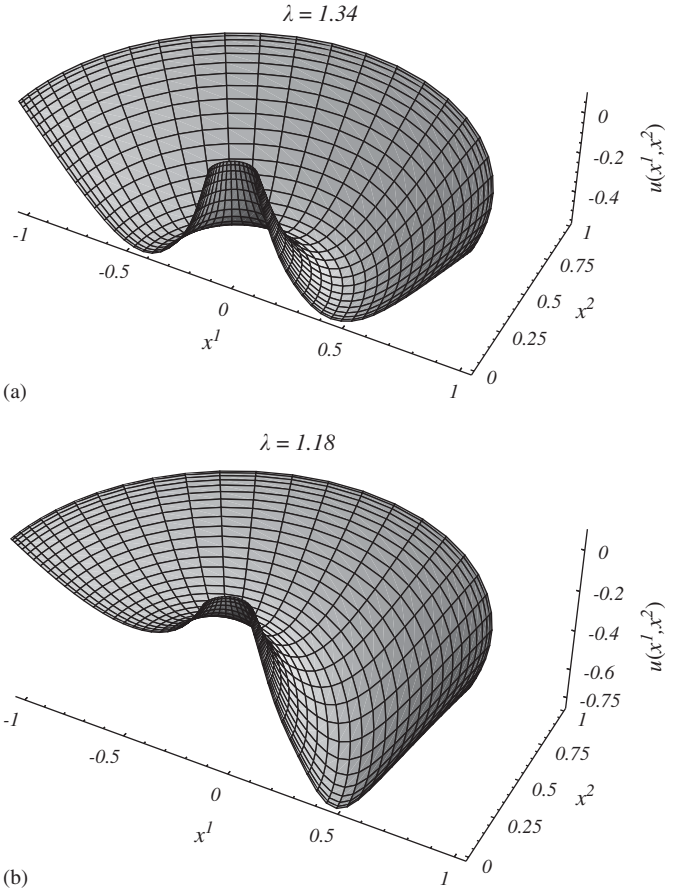

Fig. 11. (a) Symmetric and (b) asymmetric solutions for the annular disk MEMS with $\lambda = 1.34$ and $\lambda = 1.18$, respectively.

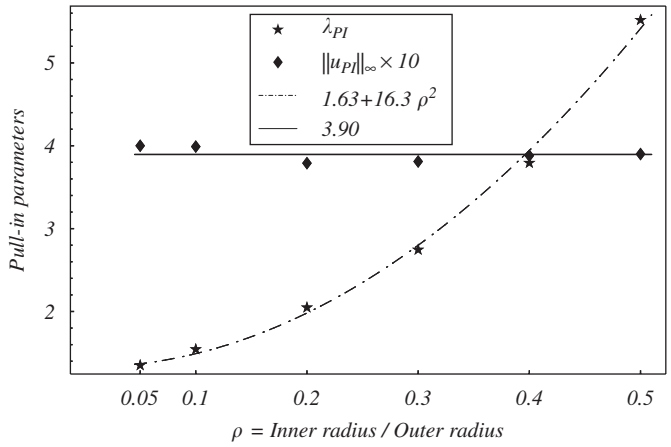

Fig. 12. Variation of pull-in parameters, λ_{PI} and $\|u_{\mathrm{PI}}\|_\infty$, with the ratio (inner radius)/(outer radius) for the annular MEMS.

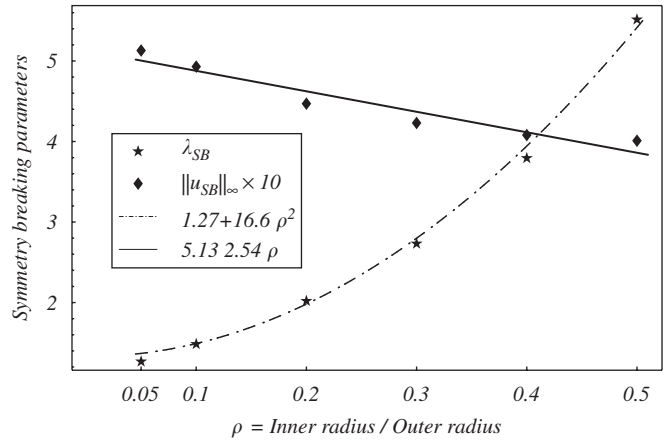

Fig. 13. Variation of symmetry breaking parameters, λ_{SB} and $\|u_{\mathrm{SB}}\|_\infty$, with the ratio (inner radius)/(outer radius) for the annular MEMS.

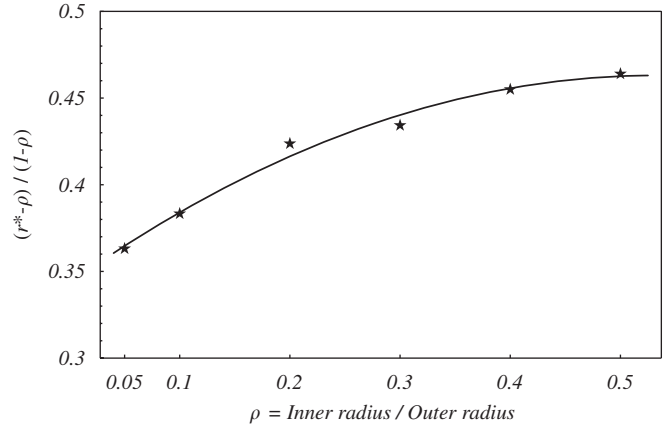

Fig. 14. Variation of the radial location of the nondimensional pull-in maximum deflection, with the ratio (inner radius)/(outer radius) for the annular MEMS.

solutions obtained by mapping the elliptic domain into a strip via the change of coordinates given in Appendix B. In elliptic coordinates, homogeneous essential boundary conditions are imposed on the edge $\xi^1 = \operatorname{arctanh}(b/a)$, and homogeneous natural boundary conditions are imposed on the remaining edges. A grid of 50×70 nodes located, respectively, along ξ^1 and ξ^2 directions is used. With a considerably reduced number of nodes (~90 versus 3500), the MLPG method is able to reproduce finite-difference results within 2% error for the nondimensional pull-in voltage, and less that 4% error for the nondimensional pull-in displacement.

Fig. 17 depicts the variation of the pull-in parameters, λ_{PI} and $\|u_{\mathrm{PI}}\|_\infty$, with the aspect ratio b/a. The nondimensional pull-in voltage data are fitted with a quadratic polynomial in a/b (dashed line), and the corresponding nondimensional pull-in maximum deflections with a straight line (solid line). Expressions for the aforementioned polynomials are

$$\lambda_{\mathrm{PI}} = 0.377\left(1 + \left(\frac{a}{b}\right)^2\right), \quad \|u_{\mathrm{PI}}\|_\infty = 0.440.$$

As the aspect ratio approaches 1, results for the elliptic geometry match results for the circular MEMS.

6. Conclusions

We have implemented the pseudoarclength continuation method in the MLPG formulation of an electrostatically actuated MEMS. A LSAWF of the problem is derived wherein essential boundary conditions are enforced by a set of Lagrange multipliers. The MLS approximation is used to generate basis functions for the trial solution, and the test functions are taken to be the weight functions of the MLS approximation. The resulting set of nonlinear equations is solved by the Newton iteration method. The accuracy and the reliability of the proposed technique is assessed through comparisons of the presently computed results with those from other numerical methods.

It is shown that a reduced number of nodes (~160) and a few steps (~100) in the pseudoarclength continuation method are sufficient for estimating the pull-in parameters and the symmetry breaking bifurcations with an error of at most 1.53%. The convergence rate of the pseudoarclength continuation method does not vanish when the pull-in state is approached; moreover, since the applied voltage is treated as unknown, the number of iterations remains bounded.

For the annular circular MEMS, the pull-in voltage increases parabolically with an increase in the ratio of the inner to the outer radius of the disk, but the maximum pull-in deflection is nearly constant. For an elliptical MEMS the pull-in voltage decreases rapidly with an increase in the ratio of the minor to the major axes of the ellipse, but the maximum pull-in deflection is essentially unchanged.

Appendix A. MLS approximation

Meshless methods generally require local interpolation to represent the trial function. In the MLPG method we

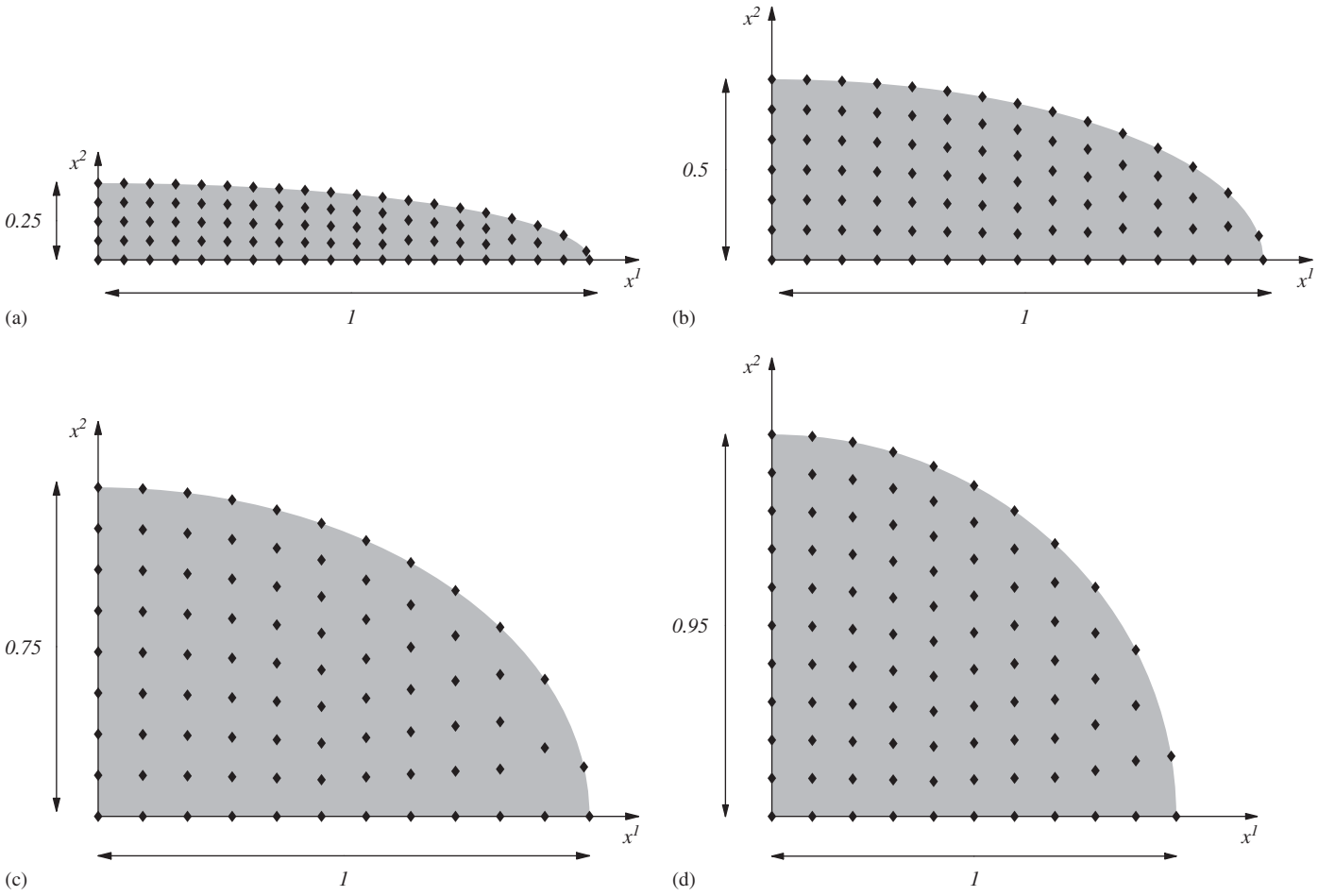

Fig. 15. Locations of (a) 86 nodes, (b) 87 nodes, (c) 85 nodes, and (d) 94 nodes on the quarter of an elliptic disk with (a) $b/a = 0.25$, (b) $b/a = 0.5$, (c) $b/a = 0.75$, and (d) $b/a = 0.95$.

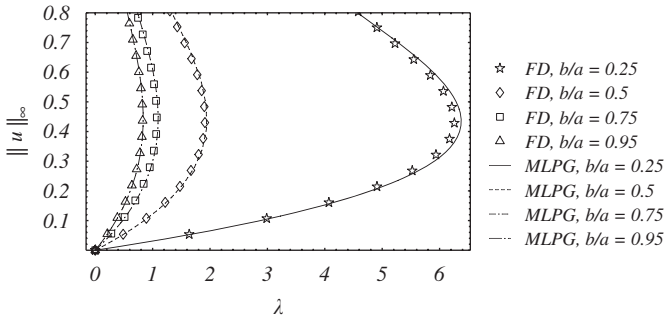

Fig. 16. Bifurcation diagram for four elliptic MEMS.

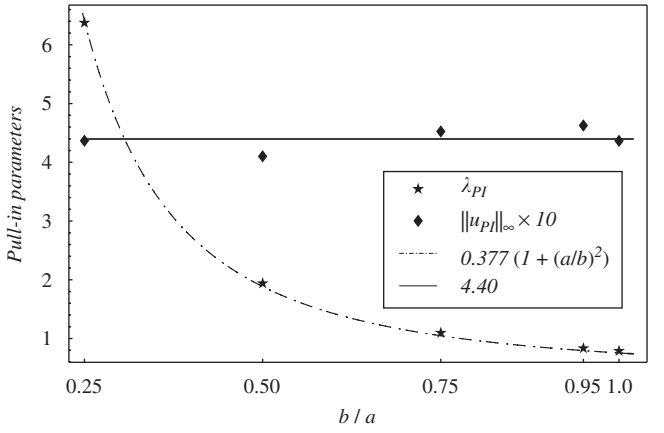

Fig. 17. Variation of pull-in parameters, λ_{PI} and $\|u_{\mathrm{PI}}\|_\infty$, with the aspect ratio b/a for the elliptic MEMS.

use the MLS approximation [35] that allows for the accurate construction of a given trial function on the entire domain, from the knowledge of its values at some, suitably chosen, scattered points.

Consider a continuous and differentiable scalar function u defined on a 2-D connected domain Ω. The generic point in Ω is indicated by $\mathbf{x}$ and its coordinates in a rectangular Cartesian frame are x^1 and x^2. The fictitious nodal values at scattered points $\mathcal{N} = \{\mathbf{x}_1, \mathbf{x}_2, \ldots, \mathbf{x}_N\}$ on $\bar{\Omega}$ are collected into the N-vector $\hat{\mathbf{w}} = [\hat{w}_1 \ \ldots \ \hat{w}_N]^{\mathrm{T}}$. The global approximation u^h on Ω of u is defined as

$$u(\mathbf{x}) \simeq u^h(\mathbf{x}) = \mathbf{p}^{\mathrm{T}}(\mathbf{x})\mathbf{a}(\mathbf{x}), \quad \mathbf{x} \in \Omega, \tag{18}$$

where

$$\mathbf{p}^{\mathrm{T}}(\mathbf{x}) = [p_1(\mathbf{x}) \ p_2(\mathbf{x}) \ \ldots \ p_m(\mathbf{x})] \tag{19}$$

is a complete monomial basis of order m.

The m-vector $\mathbf{a}(\mathbf{x}) = [a_1(\mathbf{x}) \ \ldots \ a_m(\mathbf{x})]^{\mathrm{T}}$ is composed of indeterminate coefficients, which vary with the point $\mathbf{x}$ on the domain Ω. At each location $\bar{\mathbf{x}}$ in Ω these coefficients are determined by a local least-squares approximation of $u(\mathbf{x})$ on a small neighborhood $\Omega_{\bar{\mathbf{x}}}$ of $\bar{\mathbf{x}}$. The local approximation $u_{\bar{\mathbf{x}}}(\mathbf{x})$ is defined by

$$u(\mathbf{x}) \simeq u_{\bar{\mathbf{x}}}(\mathbf{x}) = \mathbf{p}^{\mathrm{T}}(\mathbf{x})\mathbf{a}(\bar{\mathbf{x}}), \quad \mathbf{x} \in \Omega_{\bar{\mathbf{x}}} \subset \Omega. \tag{20}$$

Therefore, in a small neighborhood of a generic point $\bar{\mathbf{x}}$ the coefficients a_i are treated as the unknown constants of the classical polynomial least-squares approximation. They are determined by minimizing the functional $J_{\bar{\mathbf{x}}}$ representing the weighted discrete L^2 error norm, and defined by

$$J_{\bar{\mathbf{x}}}(\mathbf{a}) = \sum_{i=1}^{N} W_i(\bar{\mathbf{x}})[u_{\bar{\mathbf{x}}}(\mathbf{x}_i) - \hat{u}_i]^2. \tag{21}$$

The function W_i is the weight function of node i. Lower bounds for the diameters of the supports of weight functions that ensure the regularity of the MLS basis functions are given in [25].

The stationarity of $J_{\bar{\mathbf{x}}}$ with respect to $\mathbf{a}$ yields

$$\mathbf{a}(\bar{\mathbf{x}}) = \mathbf{A}(\bar{\mathbf{x}})^{-1}\mathbf{B}(\bar{\mathbf{x}})\hat{\mathbf{u}}, \tag{22}$$

where the (m,m) and the (m,N) matrices $\mathbf{A}$ and $\mathbf{B}$ are defined by

$$\mathbf{A}(\bar{\mathbf{x}}) = \mathbf{P}^{\mathrm{T}}\mathbf{W}(\bar{\mathbf{x}})\mathbf{P}, \quad \mathbf{B}(\bar{\mathbf{x}}) = \mathbf{P}^{\mathrm{T}}\mathbf{W}(\bar{\mathbf{x}}), \tag{23}$$

where $\mathbf{P}$ is a (N,m) matrix of real numbers:

$$\mathbf{P}^{\mathrm{T}} = [\mathbf{p}^{\mathrm{T}}(\mathbf{x}_1) \ \ldots \ \mathbf{p}^{\mathrm{T}}(\mathbf{x}_N)],$$

and $\mathbf{W}$ is a (N,N) diagonal matrix defined by

$$\mathbf{W}(\bar{\mathbf{x}}) = \mathrm{DIAG}[W_1(\bar{\mathbf{x}}) \ \ldots \ W_N(\bar{\mathbf{x}})].$$

Substituting (22) in the global approximation (18) gives the MLS approximation

$$u^h(\mathbf{x}) = \boldsymbol{\psi}(\mathbf{x})^{\mathrm{T}}\hat{\mathbf{u}}, \tag{24}$$

$$\boldsymbol{\psi}(\mathbf{x}) = \mathbf{p}(\mathbf{x})^{\mathrm{T}}\mathbf{A}^{-1}(\mathbf{x})\mathbf{P}^{\mathrm{T}}\mathbf{W}(\mathbf{x}), \tag{25}$$

in terms of the vector of basis functions $\boldsymbol{\psi}(\mathbf{x}) = [\psi_1(\mathbf{x}) \ \ldots \ \psi_N(\mathbf{x})]^{\mathrm{T}}$. We emphasize that for an arbitrary node i located at the place $\mathbf{x}_i$ the fictitious nodal value $\hat{u}_i$ does not equal the actual nodal value $u^h(\mathbf{x}_i)$ of the approximating function, i.e.

$$u^h(\mathbf{x}_i) \neq \hat{u}_i.$$

Indeed, the nodal values of the approximating function collected in the vector $\mathbf{u}^h$ are related to $\hat{\mathbf{u}}$ by

$$\mathbf{u}^h = \boldsymbol{\Psi}\hat{\mathbf{u}}, \tag{26}$$

where the nondiagonal matrix $\boldsymbol{\Psi}$ is defined by

$$[\boldsymbol{\Psi}]_{ij} = \psi_j(\mathbf{x}_i). \tag{27}$$

In the paper, we consider Gauss weight functions

$$W_i(\mathbf{x}) = \begin{cases} \dfrac{\exp[-(d_i/c_i)^{2k}] - \exp[-(r_i/c_i)^{2k}]}{1 - \exp[-(r_i/c_i)^{2k}]}, & 0 \leqslant d_i < r_i, \\ 0, & d_i \geqslant r_i. \end{cases} \tag{28}$$

Here, $d_i = |\mathbf{x} - \mathbf{x}_i|$ is the distance from the node located at $\mathbf{x}_i$ to point $\mathbf{x}$; c_i and k are constants controlling the shape of the weight function, and r_i is the radius of the compact support of W_i. Computed results depend upon values assigned to c_i, r_i and k.

Appendix B. Confocal elliptic coordinates

For elliptic MEMS problems solved with the finite-difference method, elliptic coordinates (ξ^1, ξ^2) are introduced. They are related to rectangular Cartesian coordinates (x^1, x^2) by

$$x^1 = c\cosh\xi^1\cos\xi^2, x^2 = c\sinh\xi^1\sin\xi^2,$$
$$\xi^1 \in \left[0, \operatorname{arctanh}\left(\frac{b}{a}\right)\right], \ \ \xi^2 \in [0, 2\pi), \tag{29}$$

where $c^2 = a^2 - b^2$, and a and b are the semi-major and the semi-minor axes of the ellipse, respectively. Thus, the elliptic domain becomes a strip. Curves $\xi^1 = \text{const.}$ are confocal ellipses with the focal points located in $x^1 = \pm c$; similarly, curves $\xi^2 = \text{const.}$ are confocal hyperbolas.

In elliptic coordinates, the Laplacian of a scalar field $u : [0, \operatorname{arctanh}(b/a)] \times [0, 2\pi) \to \mathbb{R}$ becomes (see [40])

$$\triangle u = \left[\frac{2}{c^2(\cosh 2\xi^1 - \cos 2\xi^2)}\left(\frac{\partial^2}{(\partial\xi^1)^2} + \frac{\partial^2}{(\partial\xi^2)^2}\right)\right]u. \tag{30}$$

References

[1] Taylor GI. The coalescence of closely spaced drops when they are at different electric potentials. Proc Roy Soc A 1968;306:423–34.

[2] Nathanson HC, Newell WE, Wickstrom RA, Davis JR. The resonant gate transistor. IEEE Trans Electron Devices 1967;14:117–33.

[3] Hung ES, Senturia SD. Extending the travel range of analog-tuned electrostatic actuators. J Micro-electromechanical Syst 1999;8(4): 497–505.

[4] Tilmans HA, Legtenberg R. Electrostatically driven vacuum-encapsulated polysilicon resonators: Part II. Theory and Performance. Sensors Actuators A 1994;45:67–84.

[5] Nguyen CTC, Katehi LPB, Rebeiz GM. Micromachined devices for wireless communications. Proc IEEE 1998;86(8):1756–68.

[6] Pamidighantam S, Puers R, Baert K, Tilmans HAC. Pull-in voltage analysis of electrostatically actuated beam structures with fixed-fixed and fixed-free end conditions. J Micromechanics Microengineering 2002;12:458–64.

[7] Pelesko JA. Mathematical modeling of electrostatics MEMS with tailored dielectric properties. SIAM J Appl Math 2002;62(3):888–908.

[8] Francais O, Dufour I. Normalized abacus for the global behavior of diaphragms: pneumatic, electrostatic, piezoelectric or electromagnetic actuation. J Modeling Simulation Microsystems 1999;2:149–60.

[9] Zhao X, Abdel-Rahman EM, Nayfeh AH. A reduced-order model for electrically actuated microplates. J Micromechanics Microengineering 2004;14:900–6.
[10] Na TY. Computational methods in engineering boundary value problems. New York: Academic Press; 1979.
[11] Pelesko JA. Multiple solutions in electrostatic MEMS, Proceedings of modeling and simulations of microsystems 2001. pp. 290–3.
[12] Pelesko JA, Bernstein BH, McCuan J. Symmetry and symmetry breaking in electrostatics MEMS. Proceedings of modeling and simulation of microsystems, San Francisco, CA 2003. pp. 304–7.
[13] Bao Z, Mukherjee S. Electrostatic BEM for MEMS with thin conducting plates and shells. Eng Anal Boundary Elem 2004;28: 1427–35.
[14] Chyuan S-W, Liao Y-S, Chen J-T. Computational study of the effect of finger width and aspect ratios for the electrostatic levitating force of MEMS combdrive. J Micro-electromechanical Syst 2005;14(2):305–12.
[15] Belytschko T, Lu YY, Gu L. Element-free Galerkin methods. Int J Numer Methods Eng 1994;37:229–56.
[16] Duarte CAM, Oden JT. Hp clouds—an hp meshless method. Numer Methods Partial Differential Equations 1996;12(6):673–705.
[17] Liu WK, Jun S, Adee J, Belytschko T. Reproducing kernel particle methods for structural dynamics. Int J Numer Methods Eng 1995;38: 1655–79.
[18] Lucy LB. A numerical approach to the testing of the fission hypothesis. Astron J 1977;82(12):1013–24.
[19] Nayroles B, Touzot G, Villon P. Generalizing the finite element method: diffuse approximation and diffuse elements. Comput Mech 1992;10:307–18.
[20] Melenk JM, Babuska I. The partition of unity finite element method: basic theory and applications. Comput Methods Appl Mech Eng 1996;139:289–314.
[21] Sukumar N, Moran B, Belytschko T. The natural element method in solid mechanics. Int J Numer Methods Eng 1998;43(5):839–87.
[22] Wendland H. Piecewise polynomial, positive definite and compactly supported radial basis functions of minimal degree. Adv Comput Math 1995;4:389–96.
[23] Atluri SN, Zhu T. A new meshless local Petrov–Galerkin (MLPG) approach in computational mechanics. Comput Mech 1998;22: 2117–27.
[24] Zhang GM, Batra RC. Modified smoothed particle hydrodynamics method and its application to transient problems. Comput Mech 2004;34:137–46.
[25] Atluri SN, Shen S. The meshless local Petrov–Galerkin (MLPG) method: a simple & less-costly alternative to finite element and boundary element methods. CMES: Comput Modeling Eng Sci 2002;3(1):11–51.
[26] Gu YT, Liu GR. A meshless local Petrov–Galerkin (MLPG) method for free and forced vibration analysis of solids. Comput Mech 2001;27:188–98.
[27] Gu YT, Liu GR. A meshless local Petrov–Galerkin (MLPG) formulation for static and free vibration analysis of thin plates. CMES: Comput Modeling Eng Sci 2001;2(4):463–76.
[28] Atluri SN, Cho JY, Kim H-G. Analysis of thin beams, using the meshless local Petrov–Galerkin method, with generalized moving least squares interpolations. Comput Mech 1999;24(5):334–47.
[29] Qian LF, Batra RC, Chen LM. Analysis of cylindrical bending thermoelastic deformations of functionally graded plates by a meshless local Petrov–Galerkin method. Comput Mech 2004;33: 263–73.
[30] Qian LF, Batra RC. Transient thermoelastic deformations of a thick functionally graded plate. J Therm Stresses 2004;27:705–40.
[31] Batra RC, Porfiri M, Spinello D. Treatment of material discontinuity in two meshless local Petrov–Galerkin (MLPG) formulations of axisymmetric transient heat conduction. Int J Numer Methods Eng 2004;61:2461–79.
[32] Batra RC, Porfiri M, Spinello D. Free and forced vibrations of a segmented bar by a meshless local Petrov–Galerkin (MLPG) formulation. Computational Mechanics 2006; 10.1007/s00466-006-0049-6 (available online).
[33] Batra RC, Spinello D. Analysis of adiabatic shear bands in heat-conducting elastothermoviscoplastic materials by the meshless local Bubnov–Galerkin method, submitted for publication.
[34] Batra RC, Porfiri M, Spinello D. Electromechanical model of electrically actuated narrow microbeams. J Micro-electromechanical Syst 2006, in press.
[35] Lancaster P, Salkauskas K. Surfaces generated by moving least squares methods. Math Comput 1981;37(155):141–58.
[36] Doedel E, Keller HB, Kernevez JP. Numerical analysis and control of bifurcation problems, Part I. Int J Bifurcation Chaos 1991;1:493–520.
[37] Doedel E, Keller HB, Kernevez JP. Numerical analysis and control of bifurcation problems, Part II. Int J Bifurcation Chaos 1991;1: 745–72.
[38] Pelesko JA, Chen XY. Electrostatic deflections of circular elastic membranes. J Electrostatics 2003;57:1–12.
[39] Degani-Bochobza O, Elata D, Nemirovsky Y. An efficient DPIE algorithm for CAD of electrostatically actuated MEMS devices. J Micro-electromechanical Syst 2002;11(5):612–20.
[40] Bowen RM, Wang C-C. Introduction to vectors and tensors, vol. 2. New York and London: Plenum Press; 1976.
[41] Andreaus U, Batra RC, Porfiri M. Vibrations of cracked beams using meshless local Petrov–Galerkin method. CMES: Comput Modeling Eng Sci 2005;9(2):111–32.